Available online at www.sciencedirect.com

ScienceDirect

Ceramics International 39 (2013) 9351–9359

CERAMICS INTERNATIONAL

www.elsevier.com/locate/ceramint

A comparative study of conventionally sintered, microwave sintered and hot isostatic press sintered NZP and CZP structures interacted with fluoride

Ambarish Dey[a], Amit Das Gupta[a], Debrata Basu[a], Ritu D. Ambashta[b,*], Piaray Kishan Wattal[b], Sanjiv Kumar[c], Debasis Sen[d], S. Mazumder[d]

[a]*Bio-Ceramics and Coating Division, Central Glass and Ceramic Research Institute, Kolkata 700032, India*
[b]*Process Development Division, Bhabha Atomic Research Centre, Trombay, Mumbai 400085, India*
[c]*NCCCM/BARC, ECIL Post, Hyderabad 500062, India*
[d]*Solid State Physics Division, Bhabha Atomic Research Centre, Trombay, Mumbai 400085, India*

Received 21 December 2012; received in revised form 10 May 2013; accepted 11 May 2013
Available online 23 May 2013

Abstract

Sodium zirconium phosphate and calcium zirconium phosphate, two potential radioactive wasteforms, were treated with fluoride, and different methods of sintering were evaluated. Different compositions were prepared by adding calcium fluoride to sodium zirconium phosphate and sodium fluoride to calcium zirconium phosphate. These mixtures were calcined in a microwave furnace and then sintered. The increase in densification of the samples sintered in a hot isostatic press were observed to be nearly uniform, while other samples that were sintered in a microwave and in a resistance furnace were inhomogeneous. The concentration of inhomogeneities was higher in fluorinated samples prepared under closed conditions in a hot press than samples prepared under microwave conditions in air.

Keywords: A. Hot isostatic press; A. Sintering; Ceramics; Microwave; Nuclear wastes

1. Introduction

A process has been proposed to extract thorium from spent uranium-233 fuel from advanced heavy water reactors [1]. The stability of thorium oxide complicates its dissolution. The addition of hydrofluoric acid (HF) along with nitric acid (HNO_3) has been proposed to dissolve the wastes prior to reprocessing. The fluorides of fission products and reactor fuel components, such as ruthenium, technetium, uranium and plutonium, can have an enormous impact on the corrosion of the processing equipment. Fluoride can be stabilised in ceramics and glass ceramics [2–15] for use in laser applications and studies of dental and bone growth. Fluoridated apatite $Ca_{10}(PO_4)_6F_2$ [3,4], oxyfluoride ceramics $Ca(Ti_{1-x}Li_x)O_{3-3x}F_{3x}$ where $0 < x \leq 0.4$ [5], biphasic calcium phosphate [6], tricalcium phosphate [7] and $ZrO_2(Y_2O_3)CaF_2$–Ag [8] are some of the crystalline forms of fluoride ceramics. Examples of glass or glass–ceramics matrices include: calcium fluoride stabilised in aluminosilicate glasses [9,10], rare-earth doped CaF_2 [11,12], borosilicate glass bearing F and Ca [13,14] and apatite–mullite glass ceramics [15]. Sodium zirconium phosphate (NZP; $NaZr_2(PO_4)_3$) and calcium zirconium phosphate (CZP; $CaZr_4(PO_4)_6$) are potential candidates for the immobilisation of radioactive waste [16–17]. The present study has been undertaken to investigate the retention of fluoride in these two phosphates.

Typical solid state syntheses of NZP employ high calcination temperatures of 1100–1300 °C and long soaking times in the 12–196 h range [18–19]. The higher processing temperatures and the longer heating times lead to the loss of components from the reaction mixtures because of the volatile nature of many Na or P compounds and the formation of nonhomogeneous products with ZrP_2O_7 or ZrO_2 as a secondary phase. This necessitates the exploration of efficient alternative methods, such as microwave processing, for synthesising and sintering NZP compounds. This

*Corresponding author. Tel.: +91 22 25594120, +91 22 25595050.
E-mail address: aritu@barc.gov.in (R.D. Ambashta).

0272-8842/$ - see front matter © 2013 Elsevier Ltd and Techna Group S.r.l. All rights reserved.
http://dx.doi.org/10.1016/j.ceramint.2013.05.053

microwave method offers several advantages over conventional methods, primarily the very short time required for the reaction and sintering, and the selectivity in energy transfer from the microwave field. Several authors previously reported that microwave-assisted preparation is a suitable technology for low temperature processing [20–22]. The hot isostatic press (HIP) process subjects a sample to elevated temperature and isostatic gas pressure in a high pressure containment vessel [23–24] and enables efficient sintering.

This study compares the results from three methods of sintering mixtures of fluoride with NZP and CZP: microwave processing, hot isostatic pressing and a resistance heated furnace.

2. Experimental

2.1. Materials and synthesis methods

A CZP composition was prepared by ball milling $Ca(NO_3)_2 \cdot 4H_2O$, $ZrO(NO_3)_2 \cdot H_2O$ and $NH_4H_2PO_4$ in a Retsch-Germany High Energy Planetary Mill with acetone as the milling medium. Five additional compositions, CZPF1, CZPF2, CZPF3, CZPF4 and CZPF5, were prepared by adding 0.25, 0.50, 1.00, 2.00 and 2.50 wt% of sodium, respectively, as NaF in the CZP reaction mixture. These materials were first air dried and then oven dried at 80 °C, and the dried compositions were calcined in a 2.45 GHz microwave furnace at 700 °C for 1 h.

Similarly, an NZP composition was prepared from Na_2CO_3, $ZrO(NO_3)_2 \cdot H_2O$ and $NH_4H_2PO_4$ in a Retsch High Energy Planetary Mill with acetone [20]. Five additional compositions, NZPF1, NZPF2, NZPF3, NZPF4 and NZPF5, were prepared by adding 0.25, 0.50, 1.00, 2.00 and 2.50 wt% of CaF_2, respectively, to the NZP reaction mixtures. These materials were processed in the same manner as the CZPF samples. The microwave calcination temperature was 700 °C.

The CZPF and NZPF samples were ground with a mortar and pestle and passed through a 60-mesh sieve to form a fine powder. These powders were pelletised to form samples with a diameter of 10 mm and a height of 15 mm for the sintering studies.

2.1.1. Sintering under microwave conditions

Specimens of CZP the CZPF1, CZPF2, CZPF3, CZPF4 and CZPF5 compositions were sintered at 1100, 1200 and 1250 °C for 1 h in a 2.45 GHz microwave furnace. Specimens of NZP and the NZPF1, NZPF2, NZPF3, NZPF4 and NZPF5 compositions were sintered at 1200 °C, 1250 °C and 1275 °C under the same conditions of soaking and microwave power.

2.1.2. Sintering in a resistance heated furnace

Specimens of CZP and the five CZPF compositions were heated at 1350 °C for 2 h.

2.1.3. Sintering under hot isostatic pressing conditions

The samples made from the five compositions of CZP calcined with NaF (calcined at 700 °C) were heated under isostatic pressing conditions in an argon atmosphere at 1100 °C and 1200 °C with a soaking time of 2 h and a constant pressure of 1000 bar. This hot isostatic press was procured from Avure Technologies Pvt. Ltd., USA. The samples were fired in a molybdenum disilicide furnace. The samples made the five compositions of NZP calcined with CaF_2 (calcined at 700 °C) were also heated under the same conditions at 1100 °C and 1200 °C with a soaking time of 2 h and a constant pressure of 1000 bar.

2.2. Bulk density measurements

The bulk densities of the sintered pellet samples were measured by Archimedes' Principle using kerosene as the suspending medium. A vacuum suction pump was attached to the desiccator to produce bubbles and to soak the materials in kerosene. The suction pump was run for 1 h, and the vacuum was maintained for 12 h. The weights of the soaked and suspended samples were measured using a density metre with kerosene as the suspension medium.

2.3. Characterisation of the sintered samples

Sintered samples were characterised for their phase purity by room temperature XRD. The phase composition of the powder was analysed by X-ray diffraction (XRD, Philips Analytical, X'Pert, 1830, The Netherlands) using Cu Kα radiation at 40 kV and 30 mA. The scanning range (2θ) was from 10° to 60° at a scan rate of 1 deg/min and a step size of 0.02°.

The microstructure was observed with a LEO S 430 I Scanning Electron Microscope in backscattered electron (BSE) mode for polished surfaces and secondary electron (SE) mode for fractured surfaces.

Small-angle neutron scattering experiments were performed using a double-crystal small angle neutron scattering instrument at the Guide Tube Laboratory of the Dhruva reactor at Trombay, India [25–26]. This instrument consists of a non-dispersive (1,−1) setting of 111 reflections from single silicon crystals with the specimen between the two crystals. The scattering intensities were recorded as a function of the wave vector transfer, $q=4\pi \sin(\theta)/\lambda$, where 2θ is the scattering angle, and λ (=0.312 nm) is the incident neutron wavelength. The compacted specimens were placed on a sample holder with a circular slit with a 1 cm diameter. The measured SANS profiles were corrected for background, transmission and instrument resolution.

Fluoride content was estimated using a sensitive non-destructive method by analysing the prompt gamma rays induced with charged particles (PIGE) [27–29]. The fluorine content was determined by detecting 197 keV gamma rays produced by the $^{19}F(p, p–\gamma)^{19}F$ reaction and 6–7 MeV gamma rays emitted by the $^{19}F(p,\alpha–\gamma)^{16}O$ reaction. These measurements were carried out on thick pellets that were obtained by pelletising mixtures of the powdered samples with 10% high purity graphite powder.

3. Results and discussion

3.1. X-ray diffraction

Some characteristic X-ray diffraction patterns of samples of CZP, compositions of CZP treated with NaF, NZP and compositions of NZP treated with CaF_2 sintered in a microwave furnace at 1200 °C or in a hot isostatic press at 1200 °C and 1000 bar, are shown in Fig. 1. Comparing the XRD patterns showed that sodium zirconium phosphate (JCPDS 33-1312) was present as a principle phase in all of the samples [30–31]. The addition of fluoride to CZP or NZP did not significantly alter the XRD patterns of the isostructural CZP and NZP phases.

3.2. Bulk density

Fig. 2 shows the variation in density of CZP with different amounts of NaF after sintering at 1100 °C, 1200 °C and 1250 °C in a microwave furnace and at 1350 °C in a resistance heated furnace. For samples sintered at 1100 °C, the densification increased with the addition of 2.50% NaF, reaching a maximum bulk density of 2.80 g/cm^3. For samples sintered at 1200 °C, the densification increased with the addition of NaF up to 1.00% NaF, where the maximum bulk density was 2.80 g/cm^3, and subsequently thereafter density decreased with further addition of 2.00 and 2.50% NaF. For samples sintered at 1250 °C, the densification increased with the addition of NaF up to 0.25% NaF, where the maximum bulk density was 2.79 g/cm^3. The density decreased with the further addition of NaF up to 2.50% NaF. These results suggested that the drop in density for sintering at higher temperatures may be a result of the formation of large pores due to the presence of a transient liquid phase. A sodium-rich liquid phase formed due to the high sodium solubility in CZP, and this liquid may have penetrated the grain boundaries of CZP and formed a solid solution through solution re-precipitation. This transient liquid phase left behind large pores due to the outward diffusion of

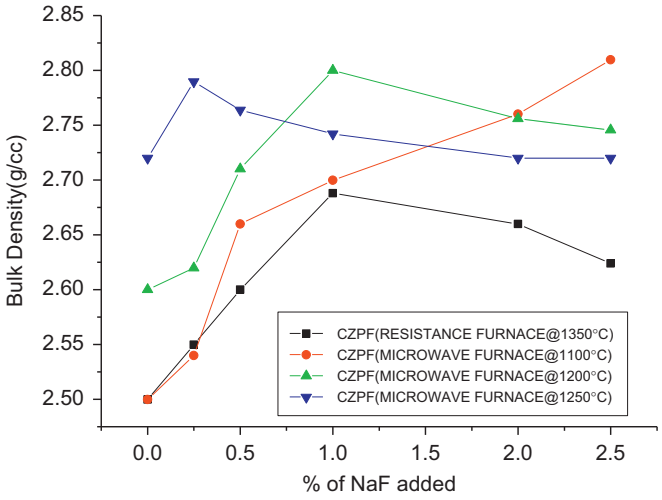

Fig. 2. Density of CZP compositions interacted with different amounts of NaF sintered in Resistance furnace at 1300° C and Microwave furnace at 1100° C, 1200° C, and 1250° C.

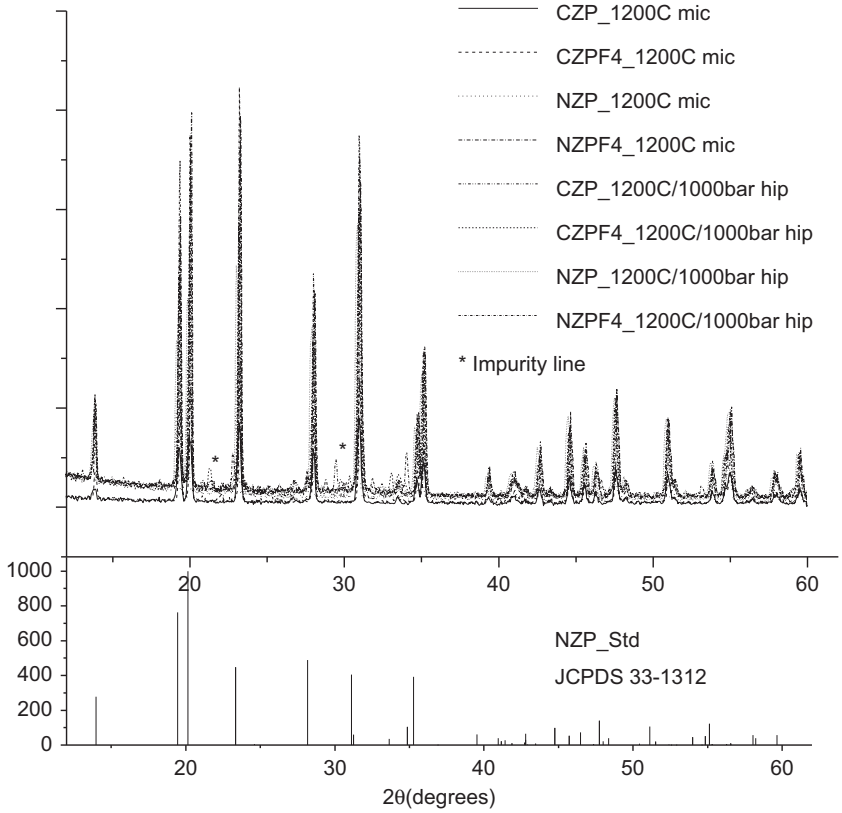

Fig. 1. XRD patterns of samples prepared under different conditions of sintering using microwave (labelled as mic) and hot isostatic press (labelled as hip).

the liquid phase into the solid matrix as the liquid phase was incorporated into the solid. The calcium zirconium phosphate structure is isostructural to the sodium zirconium phosphate structure. This may have led to the facile penetration of the sodium ions into its structure [32]. For samples sintered at 1350 °C in the resistance heated furnace, the densification increased with the addition of NaF up to 2.50% NaF, where with the maximum bulk density was 2.69 g/cm^3. Fig. 2 clearly shows the advantage of microwave sintering over sintering in a resistance heated furnace because the density was higher in the microwave heated samples. Fig. 3 shows the variation in density of NZP with different amounts of CaF_2 after sintering at 1200 °C, 1250 °C and 1275 °C in a microwave furnace and at 1350 °C in a resistance furnace. For sintering under microwave conditions, the addition of CaF_2 to NZP had a small negative effect on the densification of the materials that may be attributed to the poor solubility of CaF_2 in the NZP compositions.

Changes in the densification of CZP upon sintering with different amounts of NaF at two different temperatures, 1100 and 1200 °C, under hot isostatic pressing conditions at 1000 bar for 2 h are given in Fig. 4. Changes in the densification of NZP upon sintering with different amounts of CaF_2 at two different temperatures, 1100 and 1200 °C, under hot isostatic pressing conditions at 1000 bar for 2 h are shown in Fig. 5. For the HIP sintered samples in an argon atmosphere, there was a trend of regular increases in the bulk densities of the samples of both CZPF and NZPF. These trends in the bulk density can be attributed to the reaction under pressure and an inert atmosphere.

3.3. Microstructure

Fig. 6 shows the SEM micrographs of the polished surfaces of CZP and NaF treated CZP compositions sintered at 1200 °C in a microwave furnace. No significant difference was observed in the nature of the crystallites. Similarly, no significant change was

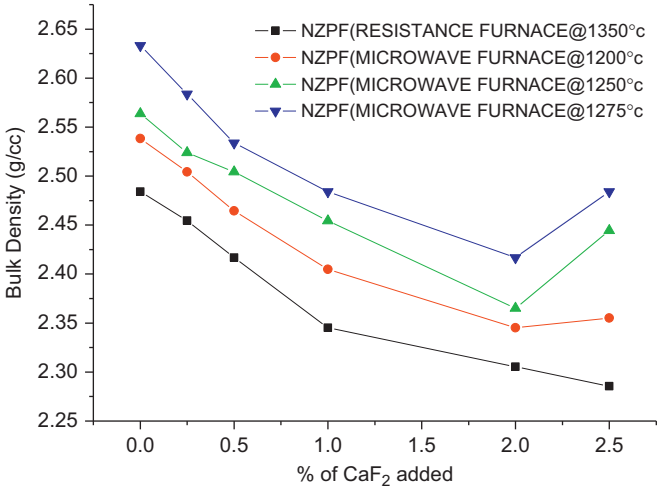

Fig. 3. Density of NZP composition interacted with different amounts of CaF_2 sintered in Resistance furnace at 1350° C and Microwave furnace at 1200° C, 1250° C, and 1275° C.

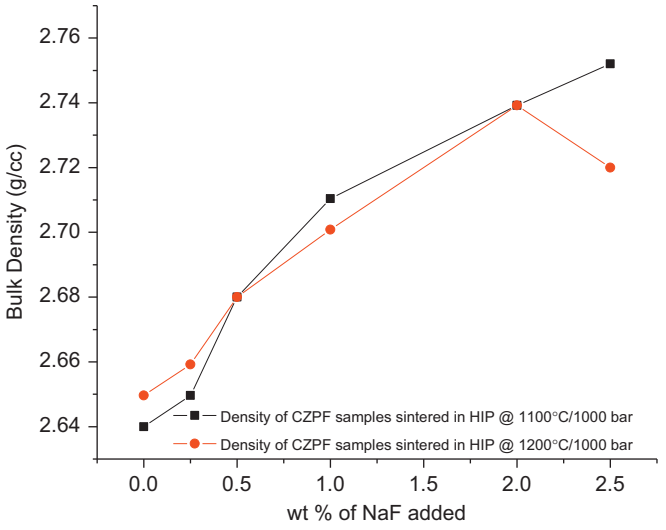

Fig. 4. Density of CZPF samples sintered in HIP at (a) 1100° C and 1000 bar pressure and (b) 1200° C and 1000 bar pressure.

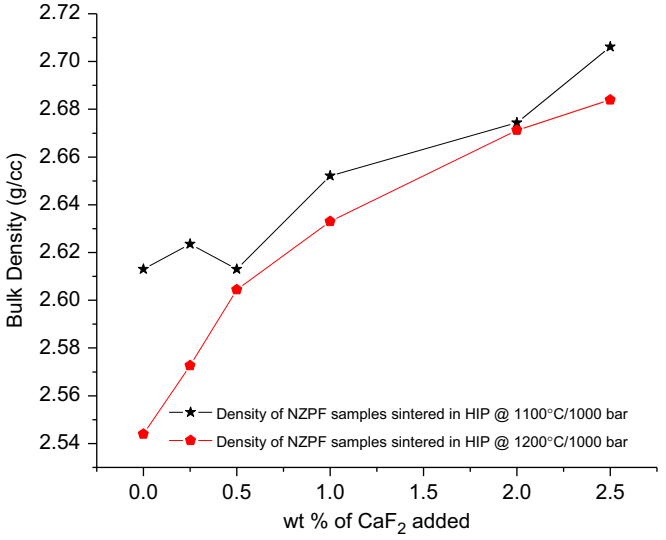

Fig. 5. Density of NZPF samples sintered in HIP at (a) 1100° C and 1000 bar and (b) 1200° C and 1000 bar.

observed in the microstructures (Fig. 7) of NZP and CaF_2 treated NZP compositions sintered at 1200 °C in a microwave furnace. The SEM micrographs of HIP sintered samples are shown in Figs. 8 and 9. These figures showed that the density increased continuously with the percentage of fluoride. In the CZPF microstructures, the crystallinity of the samples increased with the NaF content.

3.4. Small angle neutron scattering

A comparison was made between NZP and CZP sintered under different conditions to correlate the pore size distribution with the different sintering conditions. A detailed investigation was also made on the samples of CZP and fluoride treated CZP materials. Samples of green pellets, microwave sintered at

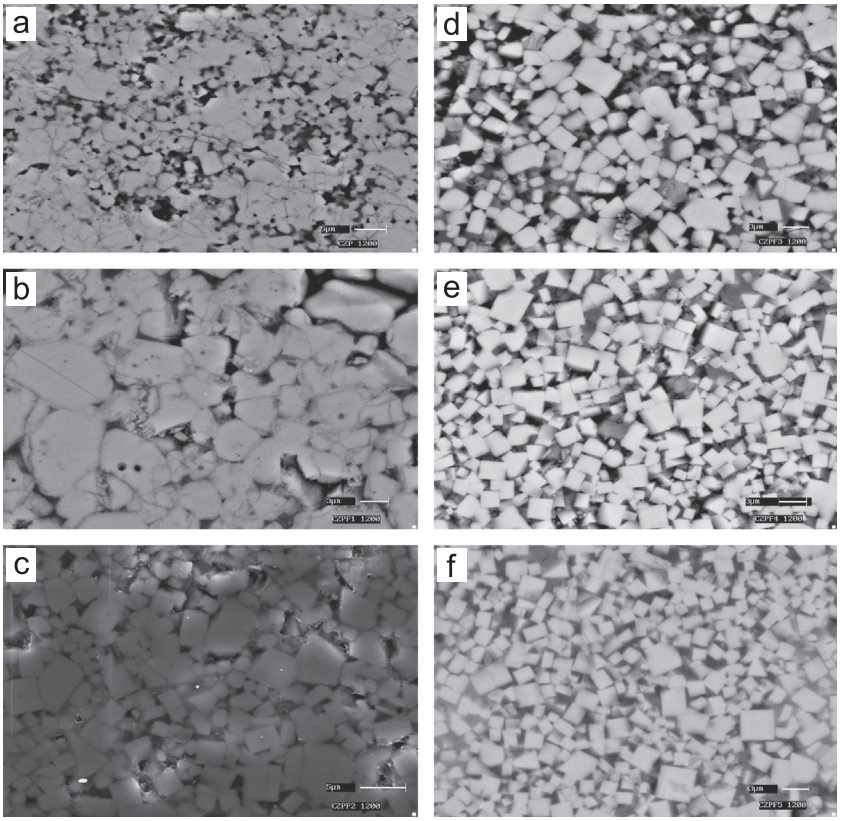

Fig. 6. SEM microstructures of CZP samples sintered in microwave furnace at 1200° C; (a) CZP, (b) CZPF1, (c) CZPF2, (d) CZPF3, (e) CZPF4, and (f) CZPF5.

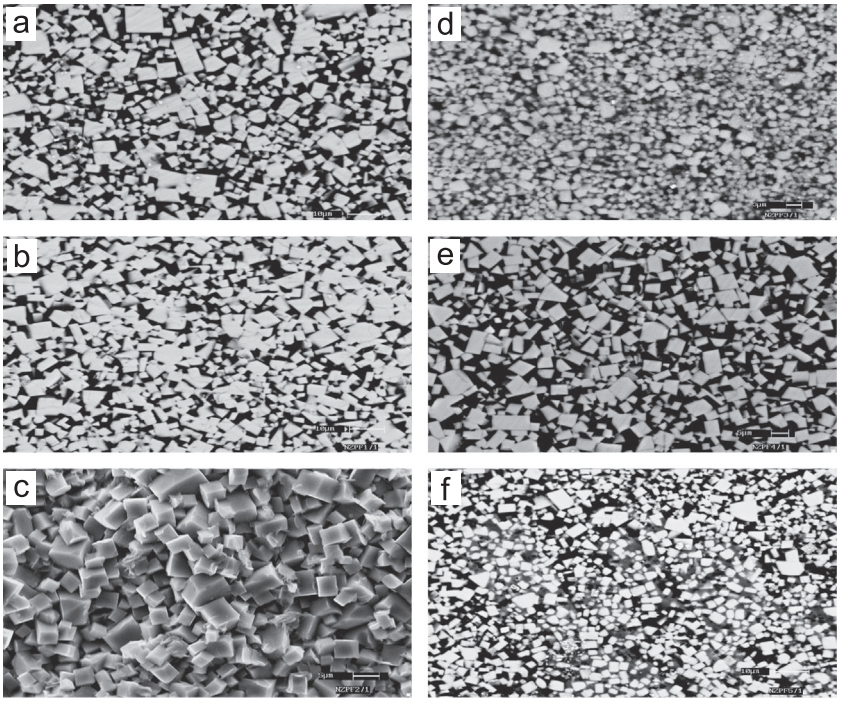

Fig. 7. SEM microstructures of NZP samples sintered in microwave furnace at 1200° C; (a) NZP, (b) NZPF1, (c) NZPF2, (d) NZPF3, (e) NZPF4, and (f) NZPF5.

1200 °C and hot isostatically compacted at 1200 °C and 1000 bar, were studied.

In each case, the SANS profiles may be broadly sub-divided in two zones, zone-I and zone-II. As the scattering space and the real space are related by Fourier transforms, the zone-I (i.e., the zone in the smaller q regime) primarily originates from the larger density fluctuations, while the zone-II (i.e., the zone in the larger q regime) primarily originates from the smaller

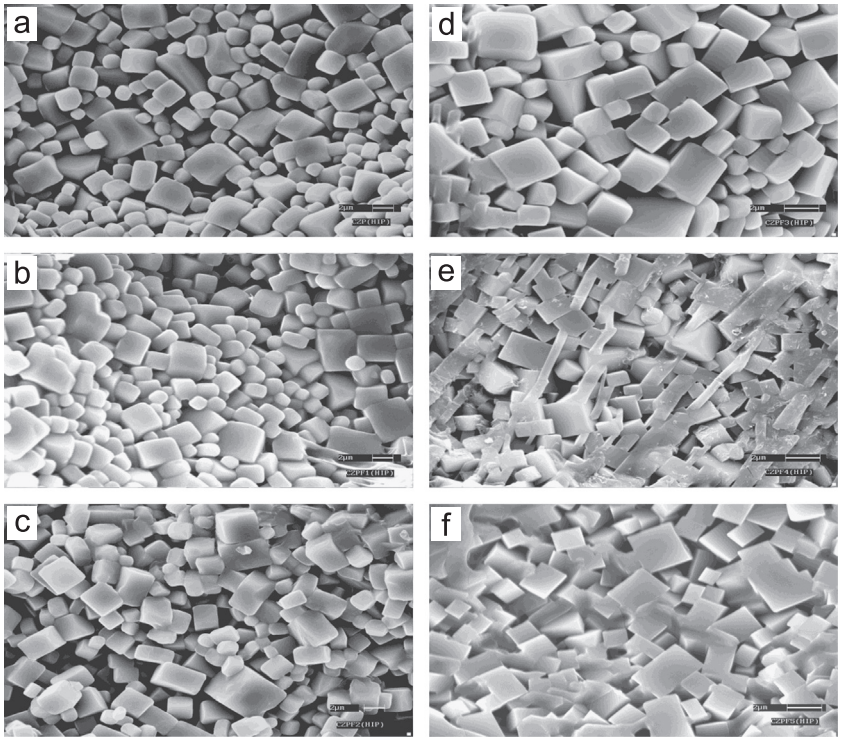

Fig. 8. SEM microstructures of CZP samples sintered in Hot Isostatic Press at 1200° C and 1000 bar pressure; (a) CZP, (b) CZPF1, (c) CZPF2, (d) CZPF3, (e) CZPF4, and (f) CZPF5.

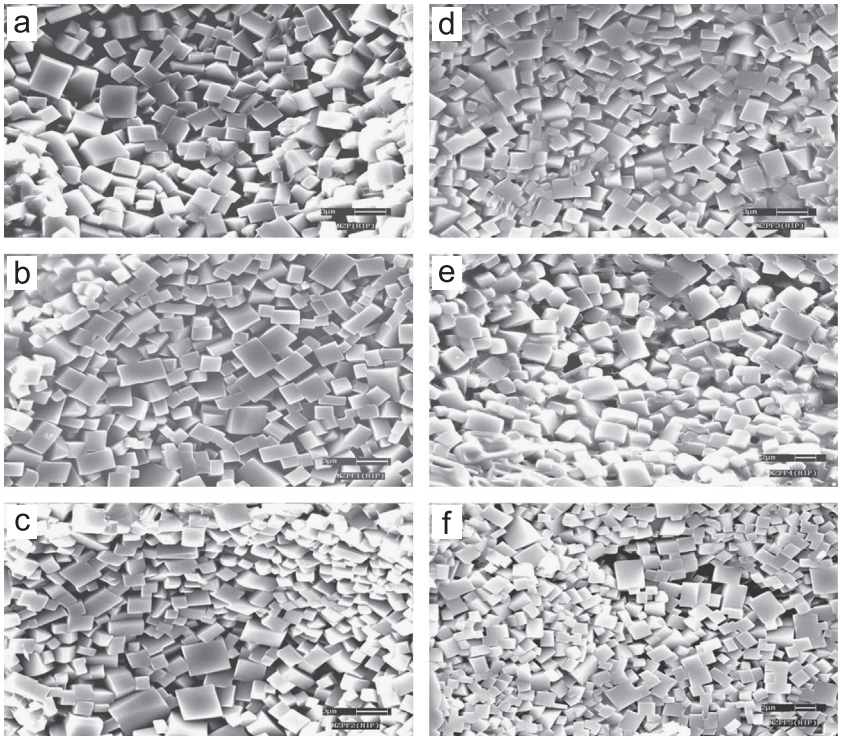

Fig. 9. SEM microstructures of NZP samples sintered in Hot Isostatic Press at 1200° C and 1000 bar pressure; (a) NZP, (b) NZPF1, (c) NZPF2, (d) NZPF3, (e) NZPF4, and (f) NZPF5.

density fluctuations. In this study, the density fluctuations have been assumed to be due to the presence of pores in the ceramic compact. To obtain real space parameters, SANS data have been modelled from the perspective of the following model. The scattering intensity from two types of density fluctuations, on widely separated length scales, may be assumed to be

$$I(q) = I_{\text{Large}}(q) + I_{\text{Small}}(q)$$

where I_1 and I_2 are scattering contributions from two length scales.

For a dilute polydisperse system,

$$I_{\text{Large}}(q) = N_{\text{Large}} \int_0^\infty P(q,R)R^6 D_{\text{Large}}(R)\, dR \text{ and}$$

$$I_{\text{Small}}(q) = N_{\text{Small}} \int_0^\infty P(q,R)R^6 D_{\text{Small}}(R)\, dR$$

where $P(q,R)$ represents the form factor of the inhomogeneities of radius R. $D_{\text{Large}}(R)$ and $D_{\text{Small}}(R)$ represent the size distribution of the inhomogeneities at larger and smaller length scales, respectively. N_{Large} and N_{Small} are proportional to the number density of the larger and smaller inhomogeneities, respectively.

In the present case, a standard lognormal distribution,

$$D(R) = \frac{1}{\sqrt{2\pi\sigma^2 R^2}} \exp\left[-\frac{[\ln(R/R_0)^2]}{2\sigma^2}\right]$$

was assumed for the inhomogeneities on both of the length scales. For this distribution, the mean, the median and the variance are expressed as $R_0\exp(\sigma^2/2)$, R_0 and $[\exp(\sigma^2)\text{-}1]$ $R_0^2\exp(\sigma^2)$, respectively. To account for the hump/peak-like feature at very low q, an inter-inhomogeneity structure factor, $S(q,R)$, was included in the scattering intensity originating from inhomogeneities at larger length scales. Thus, under the local monodisperse approximation [33], $I_{\text{Large}}(q)$ was approximated by

$$I_{\text{Large}}(q) = N_{\text{Large}} \int_0^\infty P(q,R)R^6 D_{\text{Large}}(R)S(q,R)dR$$

The range of accessible wave vector transfer, q, for the SANS experiments was 0.003–0.17 nm^{-1}. This implies a length scale range of typically 40–1000 nm in real space. A reasonably good scattering signal in this q range indeed indicates the presence of density fluctuations over the above mentioned length scale. SANS gives statistically averaged information, unlike the local information accessed by SEM at the surface. Furthermore, SANS takes into account both closed and open pores. Thus, contributions from the intra granular pores are also reflected in the SANS profile, which might not be visible in the SEM results.

Fig. 10 shows the SANS profile for NZP sintered under different conditions. The fitted parameters are tabulated in Table 1. There is very little variation in the hot compacted and

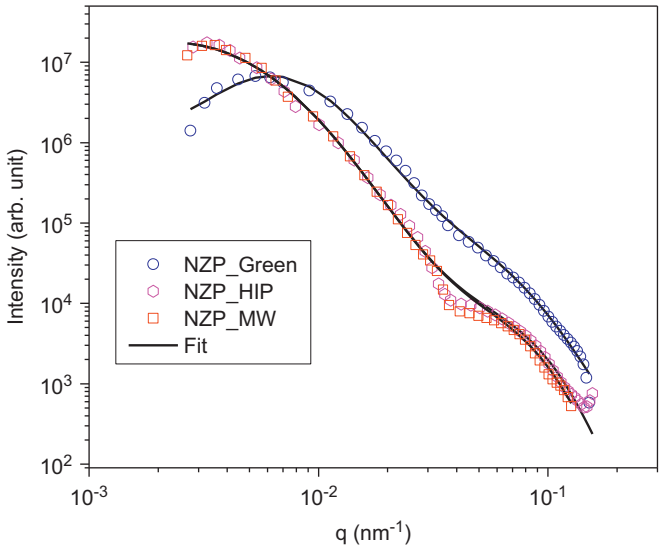

Fig. 10. SANS profile of NZP samples as green pellet CZP, microwave sintered at 1200° C and hot isostatic press compacted at 1200° C and 1000 bar.

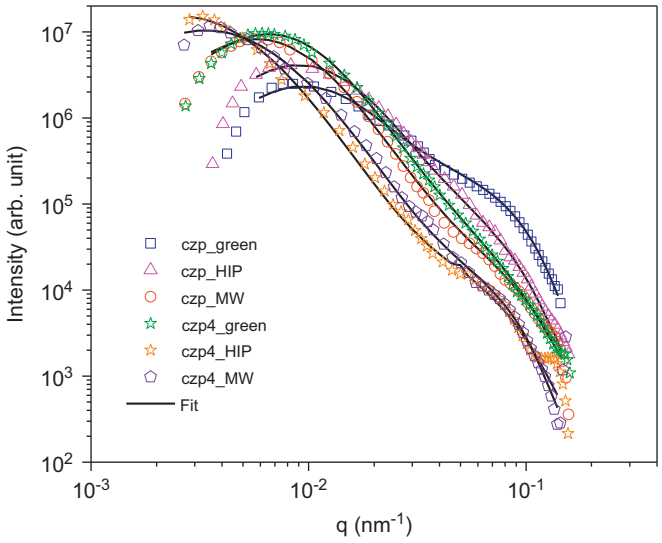

Fig. 11. SANS profile of CZP samples and 2.00 wt% fluoride interacted CZP samples as green pellet CZP, microwave sintered at 1200° C and hot isostatic press compacted at 1200° C and 1000 bar.

Table 1
Parameters obtained from fitting of the model to the experimental SANS data.

Sample	$R_{0-\text{Large}}$ (nm)	$\sigma_{0-\text{Large}}$	$R_{0-\text{Small}}$ (nm)	$\sigma_{0-\text{Small}}$	$N_{0-\text{Small}}/N_{0-\text{Large}}$	Density (g/cm^3)
CZP_Green	110.5	0.461	23.3	0.195	337.27	1.74
CZP_HIP	110.5	0.461	24.4	0.236	48.65	2.65
CZP_MW	156.9	0.478	14.9	0.368	492.30	2.60
CZP4_Green	152.4	0.461	18.1	0.362	151.51	2.50
CZP4_HIP	205.9	0.563	20.4	0.307	1094.37	2.74
CZP4_MW	154.7	0.564	26.4	0.187	158.31	2.75
NZP_Green	196.7	0.423	16.2	0.404	813.44	2.13
NZP_HIP	121.8	0.571	21.0	0.243	284.82	2.54
NZP_MW	121.8	0.571	22.1	0.243	200.43	2.54

Table 2
Wt% of fluorides estimated with the help of PIGE.

Compound	wt%
CZPF4	34.1×10^{-3}
CZPF5	50.6×10^{-3}
NZPF4	82.75×10^{-3}
NZPF5	187.55×10^{-3}

microwave sintered samples with respect to the number of inhomogeneities and the pore radii. This is also reflected in the density values, which remain practically unchanged. Fig. 11 shows the SANS profiles for CZP and CZP treated with 2 wt% fluoride under different sintering conditions. The samples sintered under hot isostatic conditions showed a reduction in the number of smaller inhomogeneities compared to larger inhomogeneities. Therefore, the density was higher for the hot isostatically sintered sample than the microwave sintered sample. For the samples treated with fluoride, this trend and the densities were reversed. The fluorides prepared under closed hot press conditions created more defects. Under microwave conditions in air, the oxygen balance reduced the small inhomogeneities.

3.5. Particle-induced gamma ray emission technique

The quantitative estimation (in wt%) of fluorides is tabulated in Table 2. A significant presence of fluorides in both the NaF-treated CZP samples and the CaF_2-treated NZP samples was observed. Consider a comparison of the data for the 2.5 wt% loading of fluoride as Ca and Na salts in NZP and CZP, respectively. The results suggest that approximately 2 wt% of the total fluoride added could be retained in the CZP structure, and 8 wt% of the total fluoride added could be retained in the NZP structure. This implies that the fluoride acceptance by the NZP structures is greater than that of the CZP structures.

4. Conclusions

The above study of the sintering of the samples showed that sintering under hot isostatic pressing conditions and the microwave assisted procedure are superior to sintering in the resistance heated furnace. The increase in densification is almost uniform in the HIP-sintered samples, but the densification is nonuniform in the samples sintered in the microwave and the resistance furnace. The fluoride is better retained in the NZP structure than in the CZP structure. The SANS profile suggests that the fluorides create more defect under the closed conditions of the hot press than under the microwave conditions in air, where the oxygen balance helps reduce the small inhomogeneities.

Acknowledgement

The investigators are grateful to BRNS, DAE, India, for funding and supporting this activity.

References

[1] B. Bhattacharjee, Paper no. IT-1, in: Proceedings of the Indian Nuclear Society of Fourteenth Annual Conference (INSAC-2003), Kalpakkam, India, December 17–19, 2003.
[2] H.K. Lee, D.K. Kim, Defect characterization of high thermal conductivity CaF_2 doped AlN ceramics by Raman spectroscopy, Modern Physics Letters B 23 (2009) 3869–3876.
[3] M.H. Fathi, E.M. Zahrani, Fabrication and characterization of fluoridated hydroxyapatite nanopowders via mechanical alloying, Journal of Alloys and Compounds 475 (2009) 408–414.
[4] G. Cho, C.N. Chau, J.P. Yesinowski, F-19 MAS NMR investigation of strontium substitution sites in Ca^{2+}/Sr^{2+} fluorapatite solid solutions, Journal of Physical Chemistry C 112 (2008) 6165–6172.
[5] H. Cherfouh, A. Mezroua, B. Melouani, L. Benziada-Taibi, DSC and dielectric investigations in new oxyfluoride ceramics $Ca(Ti_{1-x}Li_x)O_{3-3x}F_{3x}$, Euro Ceramics VII, PT 1-3: Key Engineering Materials 206 (2002) 1305–1308.
[6] Z.L. Zhu, H.Y. Yu, Q. Zeng, H.W. He, Characterization and biocompatibility of fluoridated biphasic calcium phosphate ceramics, Applied Surface Science 255 (2008) 552–554.
[7] Z. Seeley, A. Bandyopadhyay, S. Bose, Tricalcium phosphate based resorbable ceramics: Influence of NaF and CaO addition, Materials Science and Engineering 28 (2008) 11–17.
[8] J.H. Ouyang, S. Sasaki, T. Murakami, K. Umeda, Tribological properties of spark-plasma-sintered $ZrO_2(Y_2O_3)$–CaF_2–Ag composites at elevated temperatures, Wear 258 (2005) 1444–1454.
[9] S. Banijamali, B.E. Yekta, H.R. Rezaie, V.K. Marghussian, Crystallization and sintering characteristics of CaO–Al_2O_3–SiO_2 glasses in the presence of TiO_2, CaF_2 and ZrO_2, Thermochimica Acta 488 (2009) 60–65.
[10] S. Banijamah, H.R. Rezaei, B.E. Yekta, V.K. Marghussian, Sinterability, crystallization and properties of glass-ceramic tiles belonging to CaF_2–CaO–MgO–Al_2O_3–SiO_2 system, Ceramics International 33 (2007) 1557–1561.
[11] P. Aubry, A. Bensalah, P. Gredin, G. Patriarche, D. Vivien, M. Mortier, Synthesis and optical characterizations of Yb-doped CaF_2 ceramics, Optical Materials 31 (2009) 750–753.
[12] S.S. Moiseev, V.A. Petrov, S.V. Stepanov, The optical properties of high-porosity calcium fluoride ceramics, High Temperature 45 (2007) 639–644.
[13] I.W. Donald, B.L. Metcalfe, S.K. Fong, L.A. Gerrard, D.M. Strachan, R.D. Scheele, A glass-encapsulated calcium phosphate wasteform for the immobilization of actinide-, fluoride-, and chloride-containing radioactive wastes from the pyrochemical reprocessing of plutonium metal, Journal of Nuclear Materials 361 (2007) 78–93.
[14] E.E. Assem, Effect of replacing calcium oxide with calcium fluoride on some physical properties of borosilicate glass ceramics, Journal of Physics D 38 (2005) 942–945.
[15] H. Fathi, A. Johnson, R. van Noort, J.M. Ward, The influence of calcium fluoride (CaF_2) on biaxial flexural strength of apatite-mullite glass–ceramic materials, Dental Materials 21 (2005) 846–851.
[16] B.E. Scheetz, D.K. Agrawal, E. Breval, R. Roy, Waste Management 14 (1994) 489–505.
[17] R. Chourasia, O.P. Shrivastav, R.D. Ambashta, P.K. Wattal, Crystal chemistry of immobilization of fast breeder reactor (FBR) simulated waste in sodium zirconium phosphate (NZP) ceramic matrix, Annals of Nuclear Energy 37 (2010) 103–112.
[18] V.I. Petkov, A.I. Orlova, I.G. Trubach, Y.A. Asabina, V.W. Demarin, Immobilization of nuclear waste materials containing different alkali elements into single-phase NZP-based ceramics, Czechoslovak Journal of Physics 53 (2003) A639–648.
[19] A. Clearfield, R. Guerra, A. Oskarsson, M.A. Subramanlan, W. Wang, Preparation of sodium zirconium phosphates of the type $Na_{1+4x}Zr_{2-x}(P0_4)_3$, Materials Research Bulletin 18 (1983) 1561–1567.

[20] D.H. Trinh, O.C. Standard, C.C. Sorrell, Microwave heating of ceramics: a review, Journal of the Australian Ceramic Society 39 (2003) 119–129.
[21] B. Vaidyanathan, D.K. Agrawal, R. Roy, Microwave-assisted synthesis and sintering of NZP compounds, Journal of the American Ceramic Society 87 (2004) 834–839.
[22] A.H. Naik, N.V. Thakkar, S.B. Deb, A.B. Chalke, M.K. Saxena, K.L. Ramkumar, V. Venugopal, S.R. Dharwadkar, Microwave-assisted low temperature synthesis of sodium zirconium phosphate (NZP) and the leachability of some selected fission products incorporated in its structure: a case study of leachability of cesium, Journal of Chemical Sciences 122 (2010) 71–82.
[23] V.N. Zyryanov, E.R. Vance, Comparison of sodium zirconium phosphate-structured HLW forms and Synroc for high-level nuclear waste immobilization, in: W.J. Gray, I.R. Triay (Eds.). Scientific Basis for Nuclear Waste Management XX Book Series: Materials Research Society Conference Proceedings 165 (1997) 409–415.
[24] H.T. Hawkins, B.E. Scheetz, G.D. Guthrie, Preparation of monophasic sodium zirconium phosphate (NZP) radiophases: potential host matrix for the immobilization of reprocesses commercial high-level wastes, in: W.J. Gray, I.R. Triay (Eds.). Scientific Basis for Nuclear Waste Management XX Book Series: Materials Research Society Conference Proceedings 465 (1997) 387–395.
[25] S. Mazumder, D. Sen, T. Saravanan, P.R. Vijayaraghavan, Performance and calibration of the newly installed medium resolution double crystal based small-angle neutron scattering instrument at Trombay, Journal of Neutron Research 9 (2001) 39–57.
[26] S. Mazumder, D. Sen, T. Saravanan, P.R. Vijayaraghavan, A medium resolution double crystal based small-angle neutron scattering instrument at Trombay, Current Science 81 (2001) 257–262.
[27] K. Nomita Devi, H.N. Sarma, S. Kumar, Estimation of essential and trace elements in some medicinal plants by PIXE and PIGE techniques, Nuclear Instruments and Methods in Physics Research Section B 266 (2008) 1605–1610.
[28] M. Volfinger, J.L. Robert, Particle-induced-gamma-ray-emission spectrometry applied to the determination of light-elements in individual grains of granite minerals, Journal of Radioanalytical and Nuclear Chemistry Articles 185 (1994) 273–291.
[29] A.K.M. Fazlul Hoque, M. Khaliquzzaman, M.D. Hossain, A.H. Khand, Determination of fluorides in water residues by positron induced gamma emission measurements, Fluoride 35 (2002) 176–184.
[30] H. Hong, Crystal structures and crystal chemistry in the system $Na_{1+x}Zr_2Si_xP_{3-x}O_{12}$, Materials Research Bulletin 11 (1976) 173–182.
[31] S. Gali, K. Byrappa, Structure of $(Na_{2/3}Zr_{1/3})_2P_2O_7$, Acta Crystallographica C 46 (1990) 2011–2013.
[32] V.I. Petkov, A.V. Markin, I.A. Shchelokov, The heat capacity and thermodynamic functions of $Ca_{0.5}Zr_2(PO_4)_3$ crystalline phosphate from $T -> 0$ to 650 K, Russian Journal of Physical Chemistry A 84 (2010) 541–547.
[33] J.S. Pedersen, Determination of size distributions from small-angle scattering data for systems with effective hard-sphere interactions, Journal of Applied Crystallography 7 (1994) 595–608.